Temperature-driven changes in the Fermi surface of graphite

Laxman R. Thoutam,[1,2] Samuel E. Pate,[1,3] Tingting Wang,[4] Yong-Lei Wang,[4,*] Ralu Divan,[5] Ivar Martin,[1] Adina Luican-Mayer,[6] Ulrich Welp,[1] Wai-Kwong Kwok,[1] and Zhi-Li Xiao[1,3,†]

[1]*Materials Science Division, Argonne National Laboratory, Argonne, Illinois 60439, USA*

[2]*Department of Electronics and Communications Engineering, SR University, Warangal, Telangana 506371, India*

[3]*Department of Physics, Northern Illinois University, DeKalb, Illinois 60115, USA*

[4]*Research Institute of Superconductor Electronics, School of Electronic Science and Engineering, Nanjing University, Nanjing 210093, China*

[5]*Center for Nanoscale Materials, Argonne National Laboratory, Argonne, Illinois 60439, USA*

[6]*Department of Physics, University of Ottawa, Ottawa, Ontario K1N 6N5, Canada*

(Received 24 May 2022; revised 15 September 2022; accepted 23 September 2022; published 10 October 2022)

We report on temperature-dependent size and anisotropy of the Fermi pockets in graphite revealed by magnetotransport measurements. The magnetoresistances (MRs) obtained in fields along the c axis obey an extended Kohler's rule, with the carrier density following the prediction of a temperature-dependent Fermi energy, indicating a change in the Fermi pocket size with temperature. The angle-dependent magnetoresistivities at a given temperature exhibit a scaling behavior. The scaling factor that reflects the anisotropy of the Fermi surface is also found to vary with temperature. Our results demonstrate that temperature-driven changes in Fermi surface can be ubiquitous and need to be considered in understanding the temperature-dependent carrier density and MR anisotropy in semimetals.

DOI: 10.1103/PhysRevB.106.155117

I. INTRODUCTION

The Fermi surface, defined in reciprocal space as the surface of Fermi energy E_F separating the occupied electron states from unoccupied ones at zero temperature, is at the very heart of our understanding of the electronic properties of metallic states [1]. For example, anisotropic magnetoresistances (MRs) of materials can arise from nonspheric Fermi surfaces [2–5]. Changes in the Fermi surface topology, i.e., the Lifshitz transition, can evoke superconductivity in a semimetal under pressure [6]. In the absence of a structural symmetry breaking and/or a magnetic phase transition, the Fermi surface in a conventional metal does not change appreciably with temperature T since E_F is typically much larger than k_BT [7]. On the other hand, one of the interesting phenomena revealed in recent research is the temperature-driven Lifshitz transition [7–27], indicative of a temperature-induced reconstruction of the Fermi surface, discovered in the type-II Weyl semimetal WTe_2 [7]. Here, we report on the temperature dependence of the Fermi surface in the absence of a Lifshitz transition in graphite and demonstrate that temperature-driven changes in the Fermi surface may be ubiquitous in a semimetal, independent of a Lifshitz transition.

While angle-resolved photoemission spectroscopy remains a powerful technique in uncovering a temperature-induced Lifshitz transition [8–13], the conventional magnetotransport approach [15–27] is another method to study Lifshitz transitions [18–20,23–27]. As demonstrated recently in the nodal line semimetal ZrSiSe [18], a Lifshitz transition can be inferred from the anomalies in the temperature dependence of the carrier density $n(T)$ and/or mobility $\mu(T)$ by analyzing the measured MR using a two-band model.

Here, we conduct magnetotransport investigations on semimetal graphite which exhibits no Lifshitz transition, i.e., without anomalies in $n(T)$ and/or $\mu(T)$. We chose graphite for the following reasons: (1) its low carrier density ($\sim 10^{18}$ cm^{-3}) [28–31] allows temperature-induced change in E_F to be discerned from the temperature dependence of the carrier density [28]; (2) graphite is a two-band system, with the possibility to avoid the complexities associated with typical multiband semimetals. Our results show that temperature-driven changes in the Fermi surface can be reflected in the temperature dependence of the carrier density [28] and MR anisotropy [32]. Magnetotransport results reveal both the temperature-induced shift of the Fermi level and change in the anisotropy of the Fermi surface in graphite. Our results demonstrate that temperature-induced changes in the Fermi surface may be expected in semimetals without a Lifshitz transition. They also indicate that temperature-induced changes in the Fermi surface need to be considered in understanding the temperature behavior of a semimetal, such as its temperature-dependent carrier density and the anisotropy of the MRs.

We first investigate the MRs obtained in magnetic fields along the c axis of the crystal and at various temperatures. We find that they follow an extended Kohler's rule [33]:

$$\mathrm{MR} = f\left(\frac{H}{n_T \rho_0}\right), \tag{1}$$

where $\mathrm{MR} = [\rho_{xx}(H) - \rho_0]/\rho_0$, n_T is the thermal factor representing the temperature dependence of the carrier density, $\rho_{xx}(H)$ and ρ_0 are the longitudinal resistivities at a magnetic

*yongleiwang@nju.edu.cn
†xiao@anl.gov

 ©2022 American Physical Society

field H and zero field at a given temperature, respectively. The good scaling of the data to the extended Kohler's rule suggests that the size of the Fermi pockets of graphite changes with temperature. We further probe the angle dependence of the magnetoresistivities at a given temperature and find it can be scaled as [32]

$$\rho_{xx}(H,\ \theta) = \rho_{xx}(\varepsilon_\theta H), \tag{2}$$

where $\varepsilon_\theta = (\cos^2\theta + \sin^2\theta/\gamma^2)^{1/2}$, with θ being the magnetic field angle with respect to the c axis of the crystal. The scaling factor γ varies from $\gamma = 56$ at $T = 2$ K to $\gamma = 20$ at $T = 300$ K. Since γ is associated with the anisotropy of the effective mass [32], its change with temperature evinces a temperature-dependent anisotropy of the Fermi surface.

II. MATERIALS AND METHODS

We measured samples that were mechanically exfoliated out of a natural graphite crystal purchased from NGS Trading & Consulting GmbH, Germany [34]. Electric contacts with well-defined separations and locations were achieved using photolithography followed by evaporation deposition of a 300–500-nm-thick Au layer with a 5-nm-thick Ti adhesion layer (see Fig. S1 in the Supplemental Material [35] for an image of the sample from which the reported data were obtained). DC four-probe resistive measurements were carried out in a Quantum Design PPMS-9 using a constant current mode ($I = 100\,\mu$A). Angular dependencies of the resistance were obtained by placing the sample on a precision, stepper-controlled rotator with an angular resolution of 0.05 °. The magnetic field is always perpendicular to the current I which flows in the ab plane of the crystal.

III. RESULTS AND DISCUSSION

Figure 1(a) (in logarithmic scale) and Fig. S2 in the Supplemental Material [35] (in linear scale) present the typical magnetic field dependence of the longitudinal resistivity $\rho_{xx}(H)$ at various temperatures. At $T = 300$ K, $\rho_{xx}(H)$ can be well described as $\rho_{xx}(H) \sim H^\alpha$ with $\alpha = 1.8$. With decreasing temperature, α becomes smaller at high fields. The occurrence of linear behavior at $T < 50$ K may reflect that the system is at the quantum limit [36–39], though the oscillations in the magnetoresistivity may originate from other mechanisms besides the Shubnikov–de Haas effect [36,37,39] (see Fig. S3 in the Supplemental Material [35] for additional experimental results and its caption for more discussion). Figure 1(b) shows the temperature dependence of the longitudinal resistivity $\rho_{xx}(T)$ at a few fixed magnetic fields, which are constructed from the measured $\rho_{xx}(H)$ curves at fixed temperatures to avoid nonequilibrium temperature effects. At zero field, the sample shows the expected metallic behavior with a residual resistivity ratio $rrr \approx 14.3$. Like those reported in Ref. [31], the curves at $H = 0.04$, 0.08, and 0.2 T exhibit the typical turn-on temperature behavior often observed in topological semimetals, i.e., $\rho_{xx}(T)$ changes from metallic to semiconductinglike behavior with decreasing temperature [31]. At $H \geqslant 0.6$ T, the curves show pure semiconductinglike behavior, which is barely seen in both topological and trivial semimetals. Another notable finding is the MR at room temperature, with a remarkable value of $MR \approx 10^4\%$ at $H = 9$ T [see Figs. 2(a) and 2(d)]. As shown in Figs. 2(b) and 2(e), the MRs also violate the Kohler's rule.

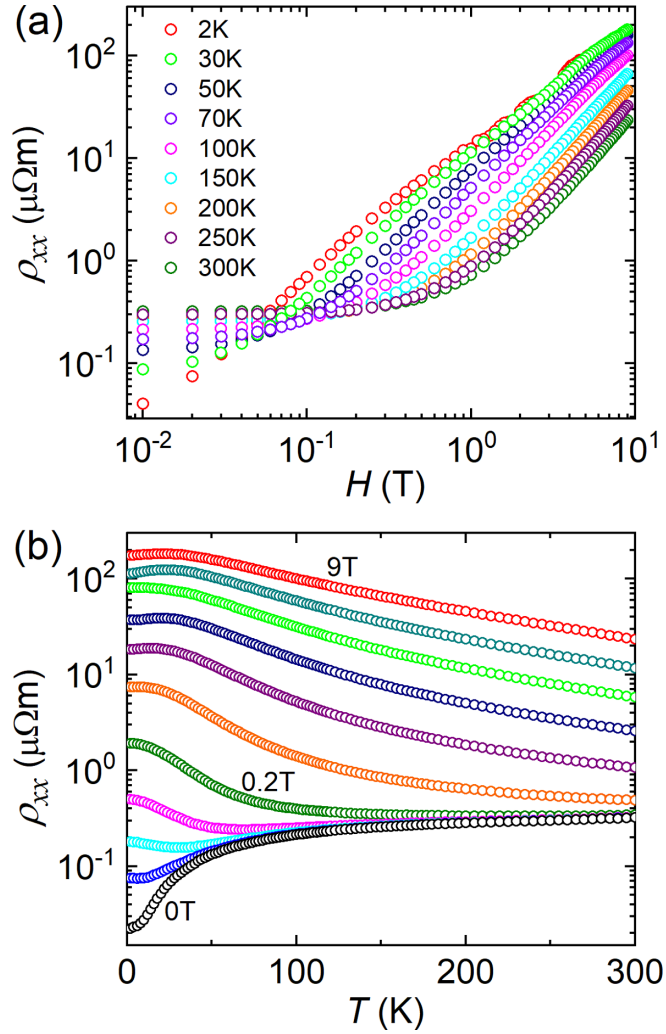

FIG. 1. Magnetoresistivities of graphite. (a) Magnetic field dependence $\rho_{xx}(H)$ measured at various temperatures. For clarity, we plot only a portion of the $\rho_{xx}(H)$ curves taken at temperatures from $T = 2$ to 120 K at intervals of 2 K, 123 to 180 K at intervals of 3 K, 184 to 200 K at intervals of 4 K, and from 205 to 300 K at intervals of 5 K. (b) Temperature dependence $\rho_{xx}(T)$ constructed from $\rho_{xx}(H)$ data. For clarity, we present $\rho_{xx}(T)$ curves at magnetic fields of $H = 0$, 0.02, 0.04, 0.08, 0.2, 0.6, 1.4, 2.6, 4.2, 6.2, and 9 T (from bottom to top). Data were taken in magnetic field parallel to the c axis of the crystal.

It is challenging to determine carrier densities in semimetals using transport measurements. Typically, they are derived by fitting the magnetoresistivities/magnetoconductivities with a two-band model [18–20,23–27]. This approach can be unreliable since most semimetals have multiple bands. For example, the MR of ZrSiSe was found to follow Kohler's rule [40], which is valid for systems with constant carrier densities, even though the existence of a Lifshitz transition in this material is inferred from anomalies in $n(T)$ using a two-band model analysis [18].

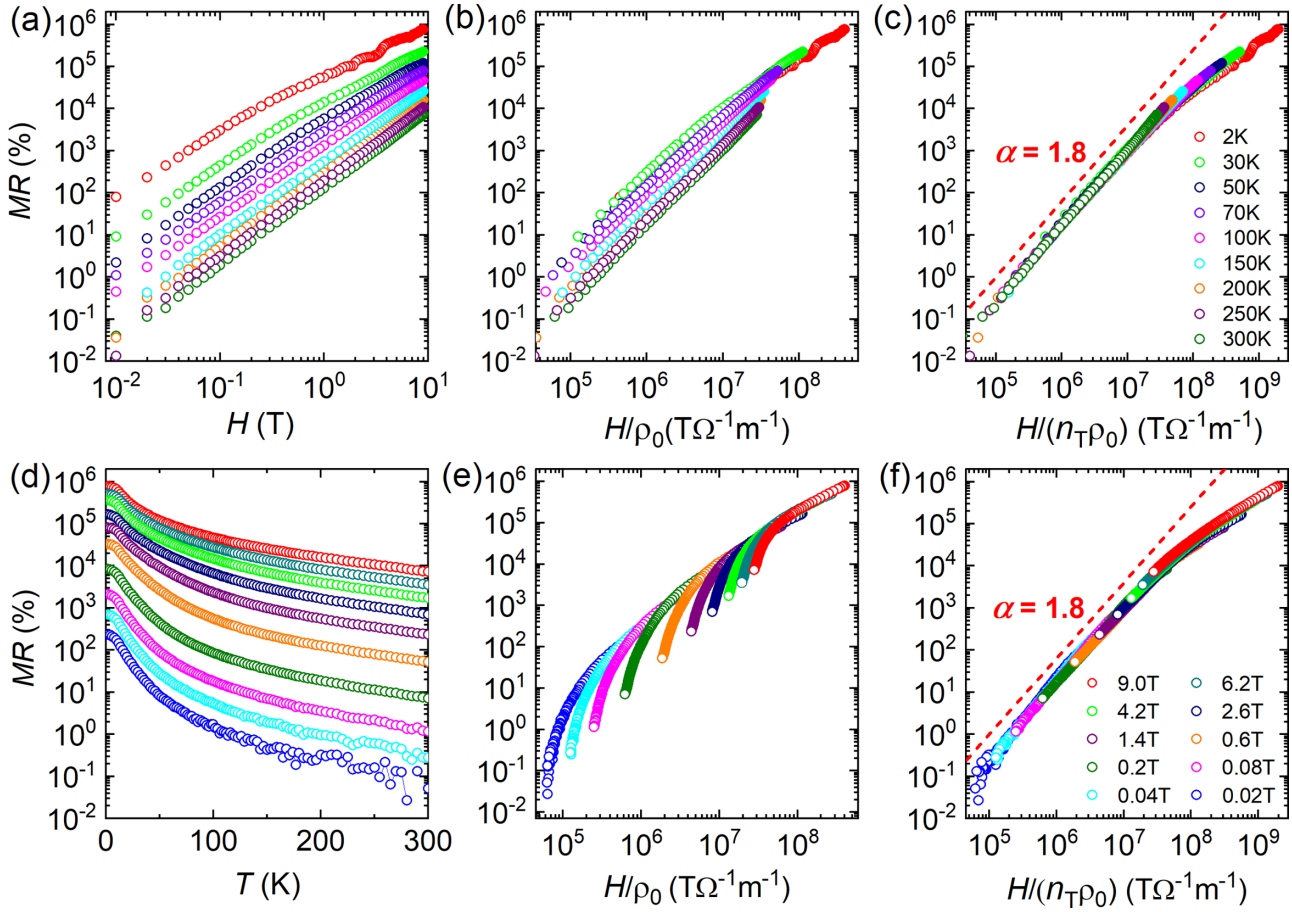

FIG. 2. Extended Kohler's rule of the magnetoresistance (MR). (a) and (d) Magnetic field and temperature dependences of the MR derived from data in Figs. 1(a) and 1(b), respectively. (b) and (e) Kohler's rule plots of the data in (a) and (d), respectively. (c) and (f) Extended Kohler's rule plots of the MR curves in (a) and (d), respectively. To be comparable with the scaling results in Fig. S6 in the Supplemental Material [35], theoretical values of n_T were calculated by normalizing the temperature-dependent carrier densities in Fig. S6 in the Supplemental Material [35] to that at $T = 300$ K, i.e., $n_T = 1$ at $T = 300$ K. Symbols in (a)–(c) are the same as those in Fig. 1(a), while the same symbols as those in Fig. 1(b) are used for (d)–(f) [see legends in (c) and (f), respectively]. Dashed red lines in (c) and (f) represent a power law relationship of MR $\sim H^{\alpha}$ with $\alpha = 1.8$.

Graphite is a two-band system with one electron pocket and two hole pockets [28]. Thus, its magnetoresistivities were expected to follow the two-band model. Indeed, $\rho_{xx}(H)$ curves along with the Hall magentoresisitivity $\rho_{xy}(H)$ curves at high temperatures ($T > 120$ K) can be described with the two-band model, as shown in Fig. S4(a) in the Supplemental Material [35] for those at $T = 300$ K. However, deviations between the fitting and experimental curves are noticeable. In fact, the $\rho_{xx} \sim H^{1.8}$ relationship shown in the inset of Fig. S2 in the Supplemental Material [35] for the experimental $\rho_{xx}(H)$ curve obtained at $T = 300$ K differs from that ($\rho_{xx} \sim H^2$) expected for a compensated two-band system. The resulting carrier densities n_e and n_h, though being close to the theoretical values, have weaker temperature dependences than the predicted one (Fig. S4(c) in the Supplemental Material [35]). The reason can be ascribed to the distribution of the carrier mass, resulting a magnetic field dependence of the exponent α in the $\rho_{xx} \sim H^{\alpha}$ relationship [28]. At $T < 120$ K, the deviations between the fitting and experimental curves become more pronounced with decreasing temperature, as shown in Fig. S4(b) in the Supplemental Material [35] for those at $T = 104$ K. For $T < 70$ K, the two-band model fails completely, probably due to quantum effects [36–39]. That is, fitting of the magnetoresistivity data with the two-band model is not a reliable method to quantitively determine the carrier density and mobility in graphite.

On the other hand, the extended Kohler's rule in Eq. (1) can reveal the temperature dependence of the carrier density if the densities and mobilities in different bands have the same/similar temperature dependences [33], which is the case in graphite, as shown in Fig. S4 in the Supplemental Material [35]. We find that both $\rho_{xx}(H)$ and $\rho_{xx}(T)$ obey Eq. (1) (see Fig. S5 in the Supplemental Material [35]), i.e., $MR = f[H/(n_T\rho_0)]$ [33], with pronounced temperature dependence of n_T. This is not a surprise since the carrier density in graphite at zero temperature n_0 ($\sim 10^{18}$ cm^{-3}) is very close to that of TaP, in which the extended Kohler's rule was established [33]. The derived temperature dependence of the carrier density n_T (see Fig. S6 in the Supplemental Material [35]) is also like that of TaP: it decreases with temperature at $T > 50$ K and saturates at lower temperatures. We find that such a n_T can be quantitatively described theoretically [28], considering

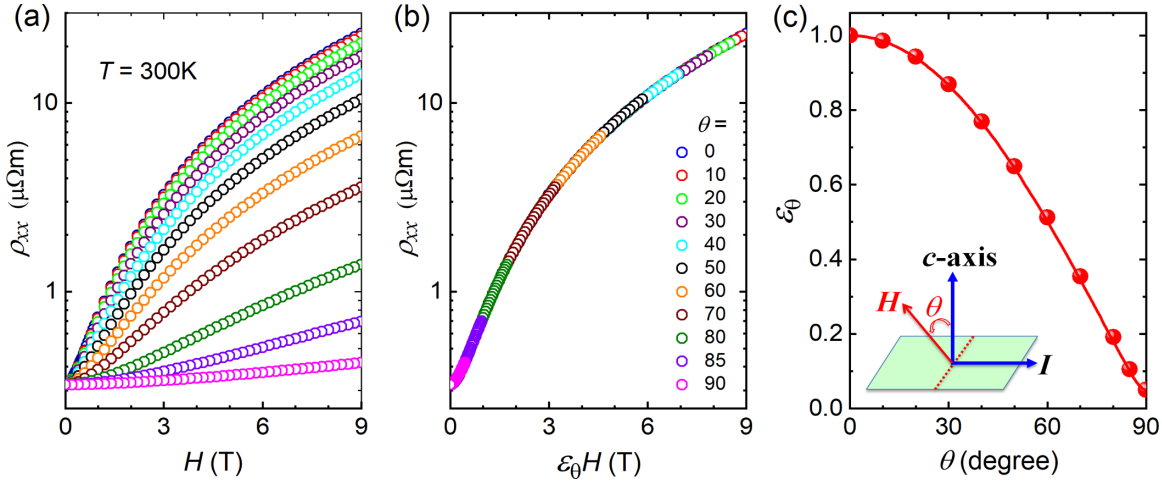

FIG. 3. Anisotropy of the magnetoresistivity in graphite. (a) $\rho_{xx}(H)$ curves at various angles θ obtained at $T = 300$ K. (b) Data in (a) replotted with H scaled by a factor ε_θ. (c) Angle dependence of the scaling factor ε_θ. Symbols are experimental data, and the solid line is a fit with $\varepsilon_\theta = (\cos^2\theta + \sin^2\theta/\gamma^2)^{1/2}$ and $\gamma = 20$. A schematic in the inset of (c) shows the definition of angle θ.

the region where the lattice scattering is dominant. The consistency of the experimental results with theory can be seen from the extended Kohler's rule plots of $\rho_{xx}(H)$ and $\rho_{xx}(T)$ using the theoretical value of n_T, as presented in Figs. 2(c) and 2(f), where n_T is obtained by normalizing the theoretical temperature-dependent carrier densities to that at $T = 300$ K (see Fig. S6 in the Supplemental Material [35]). Since n_T was calculated with a temperature-dependent Fermi energy E_F (see inset of Fig. S6 in the Supplemental Material [35]), the scaling behavior shown in Figs. 2(c) and 2(f) infers possible temperature-induced change in the size of the Fermi pockets.

The above finding led us to probe the temperature effects on the shape of the Fermi surface. Revealing the temperature-driven change in the shape of the Fermi surface can also provide additional support to the claim of temperature-dependent size. The shape of the Fermi surface is reflected in the effective mass m^* of the charge carriers, which governs the magnetoresistivity through the carrier mobility μ ($\sim 1/m^*$) [32]. Thus, we experimentally determined the anisotropy of m^* by measuring the magnetoresistivity at a given temperature with varying magnetic field orientations θ [the definition is shown in the inset of Fig. 3(c)]. Figure 3(a) shows $\rho_{xx}(H)$ curves obtained at $T = 300$ K and at various angles θ. They clearly show that the magnetoresistivity is anisotropic, with the smallest values at $H//ab$, i.e., $\theta = 90°$. Following the procedures in Ref. [32], we replot the data as $\rho_{xx} \sim \varepsilon_\theta H$ in Fig. 3(b) with the resulting ε_θ shown in Fig. 3(c). The collapse of all curves for $\theta \neq 0°$ onto the curve at $\theta = 0°$ in Fig. 3(b) follows the scaling behavior of Eq. (2), i.e., $\rho_{xx}(H,\ \theta) = \rho_{xx}(\varepsilon_\theta H)$, with $\varepsilon_\theta = (\cos^2\theta + \sin^2\theta/\gamma^2)^{1/2}$ and $\gamma = 20$, as shown in Fig. 3(c). The observed anisotropy of the magnetoresistivity and scaling behavior can be further confirmed by measuring the angle dependence of the magnetoresistivity $\rho_{xx}(\theta)$ at a particular magnetic field value H. Here, data are taken at a constant magnetic field while rotating the sample with respect to the external magnetic field, as demonstrated by $\rho_{xx}(\theta)$ curves obtained at various fields and their scaling in Figs. S7(a) and S7(b), respectively, in the Supplemental Material [35].

The temperature effects on the shape of the Fermi surface can be inferred from the temperature dependence of γ, which represents the anisotropy of the effective mass m^* for an ellipsoidal Fermi surface [32]. To reveal the temperature behavior of γ, we repeated the measurements of $\rho_{xx}(H)$ and $\rho_{xx}(\theta)$ and the associated analysis procedures for $T = 300$ K at other temperatures. As examples, we present $\rho_{xx}(H)$ data and their scaling analysis for $T = 5$ K in Fig. S8 in the Supplemental Material [35], while Fig. S9 in the Supplemental Material [35] shows $\rho_{xx}(\theta)$ data obtained at this temperature and the corresponding scaling. They clearly exhibit the high anisotropy of the magnetoresistivities and excellent scaling with Eq. (2). The derived γ shows pronounced temperature dependence, with $\gamma = 55$ at $T = 5$ K. The temperature dependence of γ is presented in Fig. 4 and exhibits a smooth decrease with increasing temperature, ranging from $\gamma = 56$ at $T = 2$ K to $\gamma = 20$ at $T = 300$ K. Interestingly, Fig. 4 also

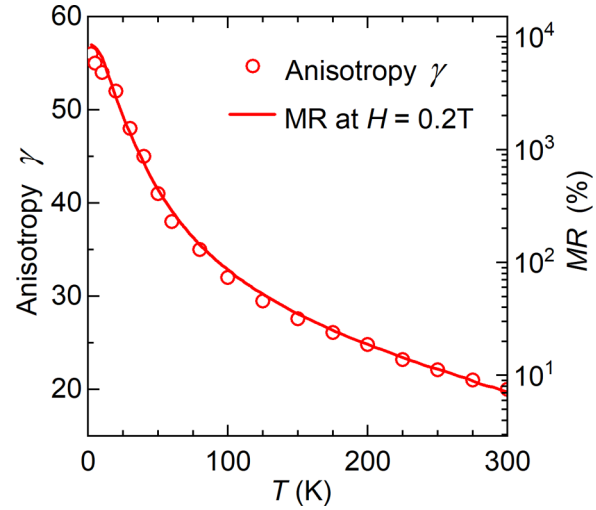

FIG. 4. Temperature dependences of the derived anisotropy factor γ (red open circles) and the magnetoresistance (MR) at $H = 0.2$ T (solid line).

shows a strong correlation between the temperature dependence of γ and that of the MR, though the overlap of $\gamma(T)$ and MR(T) may be coincidental.

Since the electron and hole bands in graphite have different densities of states, the temperature-driven shift of the Fermi level is caused by the requirement of compensation of $n_e = n_h$ at all temperatures, where n_e and n_h are the electron and hole density, respectively [28]. Pronounced temperature effects on the Fermi surface occur because the Fermi level is close to the bottom of the conduction band and the top of the valence band, i.e., the sizes of the electron and hole pockets are small. On the other hand, a typical semimetal has more than two bands, and the total density of the electrons and holes at zero temperature may differ from each other [33]. However, the changes in the electron and hole density induced by temperature must be equal, i.e., $\Delta n_e = \Delta n_h$, which can result in a temperature-dependent Fermi level if the density of states of the electron and hole bands are not the same. That is, it may be not uncommon to observe a temperature-induced shift of the Fermi level, i.e., change in the size of the Fermi pockets in semimetals. Lifshitz transition occurs when a shift of the Fermi level eventually leads to a change in the Fermi surface topology, e.g., disappearance and/or emergence of a Fermi pocket [7]. If the carrier density is low, the change in Fermi level can have a significant impact on the temperature dependence of the carrier density. In this case, the size change of the Fermi pockets may be deduced from n_T in the extended Kohler's rule of MR.

In probing the role of the quasi-2D band on the occurrence of the extremely large MR, a temperature-dependent MR anisotropy was first discovered in the type-II Weyl semimetal WTe_2 [32]. This phenomenon was later observed in both topological and trivial semimetals [15,32,41–45]. In a semimetal with multiple anisotropic Fermi pockets, such a phenomenon could occur if the temperature dependences of the carrier mobilities of different Fermi pockets are not identical. On the other hand, our results from graphite indicate that such a temperature-dependent MR anisotropy can be the direct outcome of a temperature-driven change in the anisotropy of the Fermi surface. That is, we can use the temperature-dependent anisotropy of MR, which can be obtained through convenient and widely available transport measurements, to search for possible temperature-driven changes in the anisotropy of the Fermi surface in a semimetal.

IV. CONCLUSIONS

In summary, we probed temperature effects on the Fermi surface of graphite using magnetotransport measurements. Temperature-induced size change of the Fermi pockets is inferred from the temperature dependence of the carrier density derived from the extended Kohler's rule plots of the MRs, obtained in each magnetic field orientation and at various temperatures. Temperature-driven change in the anisotropy of the Fermi pockets is revealed from the temperature-dependent anisotropy of the MR. Our results show that temperature-induced changes in the Fermi surface may be expected in semimetals. They also indicate that temperature-induced changes in the Fermi surface need to be considered in understanding the temperature behavior of a semimetal, such as the temperature-dependent carrier density and the anisotropy of the MRs. In this paper, we further demonstrate that the widely available magnetotransport measurements can be used to detect temperature effects on the Fermi surface of a semimetal through the temperature dependence of the MR anisotropy and the carrier density, with the latter being highly relevant in systems with low carrier density.

ACKNOWLEDGMENTS

This project was supported by the U.S. Department of Energy (DOE), Office of Science, Basic Energy Sciences, Materials Sciences and Engineering. S.E.P and Z.-L.X. acknowledge support by the National Science Foundation (Grant No. DMR-1901843). T.T.W and Y.-L.W. received support by the Jiangsu Excellent Young Scholar program (BK20200008). Work performed at the Center for Nanoscale Materials, a U.S. DOE Office of Science User Facility, was supported by the U.S. DOE, Office of Basic Energy Sciences, under Contract No. DE-AC02-06CH11357.

[1] S. B. Dugdale, Phys. Scr. **91**, 053009 (2016).
[2] A. Collaudin, B. Fauqué, Y. Fuseya, W. Kang, and K. Behnia, Phys. Rev. X **5**, 021022 (2015).
[3] F. Han, J. Xu, A. S. Botana, Z. L. Xiao, Y. L. Wang, W. G. Yang, D. Y. Chung, M. G. Kanatzidis, M. R. Norman, G. W. Crabtree *et al.*, Phys. Rev. B **96**, 125112 (2017).
[4] S. N. Zhang, Q. S. Wu, Y. Liu, and O. V. Yazyev, Phys. Rev. B **99**, 035142 (2019).
[5] Q. Chen, Z. F. Lou, S. N. Zhang, Y. X. Zhou, B. J. Xu, H. C. Chen, S. J. Chen, J. H. Du, H. D. Wang, J. H. Yang *et al.*, Phys. Rev. B **104**, 115104 (2021).
[6] D. Kang, Y. Zhou, W. Yi, C. Yang, J. Guo, Y. Shi, S. Zhang, Z. Wang, C. Zhang, S. Jiang *et al.*, Nat. Commun. **6**, 7804 (2015).
[7] Y. Wu, N. H. Jo, M. Ochi, L. Huang, D. Mou, S. L. Bud'ko, P. C. Canfield, N. Trivedi, R. Arita, and A. Kaminski, Phys. Rev. Lett. **115**, 166602 (2015).
[8] C. Liu, T. Kondo, R. M. Fernandes, A. D. Palczewski, E. D. Mun, N. Ni, A. N. Thaler, A. Bostwick, E. Rotenberg, J. Schmalian *et al.*, Nat. Phys. **6**, 419 (2010).
[9] Y. Zhang, C. Wang, L. Yu, G. Liu, A. Liang, J. Huang, S. Nie, X. Sun, Y. Zhang, B. Shen *et al.*, Nat. Commun. **8**, 15512 (2017).
[10] H. F. Yang, L. X. Yang, Z. K. Liu, Y. Sun, C. Chen, H. Peng, M. Schmidt, D. Prabhakaran, B. A. Bernevig, C. Felser *et al.*, Nat. Commun. **10**, 3478 (2019).
[11] S. Beaulieu, S. Dong, N. Tancogne-Dejean, M. Dendzik, T. Pincelli, J. Maklar, R. P. Xian, M. A. Sentef, M. Wolf, A. Rubio *et al.*, Sci. Adv. **7**, eabd9275 (2021).
[12] R. J. Kirby, L. Muechler, S. Klemenz, C. Weinberg, A. Ferrenti, M. Oudah, D. Fausti, G. D. Scholes, and L. M. Schoop, Phys. Rev. B **103**, 205138 (2021).
[13] M. Yang, Y. D. Liu, W. Zhou, C. Liu, D. Mu, Y. Liu, J. Wang, W. Hao, J. Li, J. Zhong *et al.*, ACS Nano **16**, 3036 (2022).

[14] F. C. Chen, H. Y. Lv, X. Luo, W. J. Lu, Q. L. Pei, G. T. Lin, Y. Y. Han, X. B. Zhu, W. H. Song, and Y. P. Sun, Phys. Rev. B **94**, 235154 (2016).
[15] Q. Zhou, D. Rhodes, Q. R. Zhang, S. Tang, R. Schonemann, and L. Balicas, Phys. Rev. B **94**, 121101(R) (2016).
[16] H. Chi, C. Zhang, G. D. Gu, D. E. Kharzeev, X. Dai, and Q. Li, New. J. Phys. **19**, 015005 (2017).
[17] Y. Liu, Y.-F. Liu, X. Gui, C. Xiang, H.-B. Zhou, C.-H. Hsu, H. Lin, T.-R. Chang, W. Xie, and S. Jia, Proc. Natl. Acad. Sci. USA **117**, 15517 (2020).
[18] F. C. Chen, Y. Fei, S. J. Li, Q. Wang, X. Luo, J. Yan, W. J. Lu, P. Tong, W. H. Song, X. B. Zhu *et al.*, Phys. Rev. Lett. **124**, 236601 (2020).
[19] S. Y. Back, Y.-K. Kim, H. Cho, M.-K. Han, S.-J. Kim, and J. S. Rhyee, ACS Appl. Energy Mater. **3**, 3628 (2020).
[20] L. S. Sharath Chandra, S. K. Ramjan, S. Banik, A. Sagdeo, and M. K. Chattopadhyay, Appl. Phys. Lett. **118**, 143905 (2021).
[21] K. Kang, W. J. Kim, D. Kim, S. Kim, B. Ji, D. H. Keum, S. Cho, Y.-M. Kim, S. Lebègue, and H. Yang, Adv. Mater. **33**, 2005742 (2021).
[22] J. Song, M. Song, Z. Li, J. Wang, Y. Wang, L. Zhang, Y. Han, L. Cao, Y. Xiong, and D. Liu, Phys. Rev. B **103**, 165141 (2021).
[23] X. Wang, D. Pan, Q. Zeng, X. Chen, H. Wang, D. Zhao, Z. Xu, Q. Yang, J. Deng, T. Zhai *et al.*, Nanoscale **13**, 2601 (2021).
[24] X. C. Yang, X. Luo, J. J. Gao, Z. Z. Jiang, W. Wang, T. Y. Wang, J. G. Si, C. Y. Xi, W. H. Song, and Y. P. Sun, Phys. Rev. B **104**, 155106 (2021).
[25] Y. Jian, Q. S. Wu, M. Yang, Q. Feng, J. X. Duan, D. Y. Chen, Q. S. Wang, W. D. Xiao, Y. G. Shi, O. V. Yazyev *et al.*, 2D Mater. **8**, 015020 (2021).
[26] E. Cheng, W. Xia, X. Shi, H. Fang, C. Wang, C. Xi, S. Xu, D. C. Peets, L. Wang, H. Su *et al.*, Nat. Commun. **12**, 6970 (2021).
[27] K. Majhi, V. Kakani, R. Ganesan, and P. S. Anil Kumar, Appl. Phys. Lett. **120**, 093105 (2022).
[28] S. Ono and K. Sugihara, J. Phys. Soc. Jpn. **21**, 861 (1966).
[29] R. O. Dillon, I. L. Spain, J. A. Woollam, and W. H. Lowrey, J. Phys. Chem. Solids **39**, 907 (1978).
[30] A. Grüneis, C. Attaccalite, T. Pichler, V. Zabolotnyy, H. Shiozawa, S. L. Molodtsov, D. Inosov, A. Koitzsch, M. Knupfer, J. Schiessling *et al.*, Phys. Rev. Lett. **100**, 037601 (2008).
[31] X. Du, S.-W. Tsai, D. L. Maslov, and A. F. Hebard, Phys. Rev. Lett. **94**, 166601 (2005).
[32] L. R. Thoutam, Y. L. Wang, Z. L. Xiao, S. Das, A. Luican-Mayer, R. Divan, G. W. Crabtree, and W. K. Kwok, Phys. Rev. Lett. **115**, 046602 (2015).
[33] J. Xu, F. Han, T.-T. Wang, L. R. Thoutam, S. E. Pate, M. D. Li, X. F. Zhang, Y.-L. Wang, R. Fotovat, U. Welp *et al.*, Phys. Rev. X **11**, 041029 (2021).
[34] NGS Trading & Consulting GmbH, https://www.graphit.de/en.
[35] See Supplemental Material at http://link.aps.org/supplemental/10.1103/PhysRevB.106.155117 for an optic image of the sample and additional experimental data and analysis.
[36] Y. Kopelevich, J. H. S. Torres, R. R. da Silva, F. Mrowka, H. Kempa, and P. Esquinazi, Phys. Rev. Lett. **90**, 156402 (2003).
[37] Y. Kopelevich and R. R. da Silva, Int. J. Mod. Phys. B **23**, 2723 (2009).
[38] Y. F. Zhao, H. W. Liu, C. L. Zhang, H. C. Wang, J. F. Wang, Z. Q. Lin, Y. Xing, H. Lu, J. Liu, Y. Wang *et al.*, Phys. Rev. X **5**, 031037 (2015).
[39] C. W. Rischau, S. Wiedmann, G. Seyfarth, D. LeBoeuf, K. Behnia, and B. Fauqué, Phys. Rev. B **95**, 085206 (2017).
[40] J. P. Song, J. Wang, Y. H. Wang, L. Zhang, M. Song, Z. H. Li, L. Cao, D. Y. Liu, and Y. M. Xiong, J. Appl. Phys. **131**, 065106 (2022).
[41] O. Pavlosiuk, M. Kleinert, P. Swatek, D. Kaczorowski, and P. Wiśniewski, Sci. Rep. **7**, 12822 (2017).
[42] N. Kumar, C. Shekhar, M. X. Wang, Y. L. Chen, H. Borrmann, and C. Felser, Phys. Rev. B **95**, 155128 (2017).
[43] J. H. Du, Z. F. Lou, S. N. Zhang, Y. X. Zhou, B. J. Xu, Q. Chen, Y. Q. Tang, S. J. Chen, H. C. Chen, Q. Q. Zhu *et al.*, Phys. Rev. B **97**, 245101 (2018).
[44] X. R. Zhang, V. Kakani, J. M. Woods, J. J. Cha, and X. Y. Shi, Phys. Rev. B **104**, 165126 (2021).
[45] O. Pavlosiuk, P. W. Swatek, J.-P. Wang, P. Wisniewski, and D. Kaczorowski, Phys. Rev. B **105**, 075141 (2022).